Nano Energy 71 (2020) 104644

Contents lists available at ScienceDirect

Nano Energy

journal homepage: http://www.elsevier.com/locate/nanoen

Full paper

Reviving reversible anion redox in 3*d*-transition-metal Li rich oxides by introducing surface defects

Yi Pei [a,b,1], Qing Chen [a,c,1], Meiyu Wang [d,1], Bin Li [b], Peng Wang [d], Graeme Henkelman [c], Liang Zhen [a,**], Guozhong Cao [b,***], Cheng-Yan Xu [a,*]

[a] School of Materials Science and Engineering, And MOE Key Laboratory of Micro-Systems and Micro-Structures Manufacturing, Harbin Institute of Technology, Harbin, 150001, China

[b] Department of Materials and Engineering, University of Washington, Seattle, WA, 98195-2120, USA

[c] Department of Chemistry and the Oden Institute for Computational Engineering and Sciences, The University of Texas at Austin, Austin, TX, 78712-0165, United States

[d] National Laboratory of Solid State Microstructures, College of Engineering and Applied Sciences, Collaborative Innovation Center of Advanced Microstructures and Center for the Microstructures of Quantum Materials, Nanjing University, Nanjing, 210093, China

ARTICLE INFO

Keywords:
Lithium-ion batteries
Li-rich layered oxides
Anion redox
Defect engineering

ABSTRACT

The reversible anion redox of $O^{2-}/(O_2)^{n-}$ in 3*d*-transition-metal based Li layered oxides (LLO) has received renewed attention due to its capability of hosting additional redox centers, which can further improve the energy density of Li-ion batteries. However, over-oxidized $(O_2)^{n-}$ was found to be unstable upon cycling, resulting in an irreversible crystal structure transformation that lowers long-term cycling stability. Herein, we demonstrated that the anion redox can be tuned through surface defect engineering, which consequently improves the cycling instability. By reconstructing the atomic configuration of the surface, a highly defective surface layer with oxygen vacancies is achieved, substantially enhancing the reversibility of anion redox as well as the stability of bulk crystal structure. The modified LLO expresses a high performances of discharge capacity (94.5%), redox potential (>3.0 V during discharge) and energy density (90.2%) after 100 cycles. *Ex-situ* XPS measurements confirm a high reversibility of the $O^{2-}/(O_2)^{n-}$ redox couple, which is supported by DFT calculations showing that the oxygen vacancies formed at the fully lithiated state of LLO mitigate the over-oxidization of oxygen and the formation of unstable superoxides ($(O_2)^-$) through a reductive coupling mechanism.

1. Introduction

Secondary batteries, especially lithium ion batteries (LIBs), have been widely applied in portable electronic equipment, hybrid electric vehicles (HEVs) and electric vehicles (EVs) since 1990s [1,2]. However, restricted largely by the energy density of current battery systems, and especially due to the limited energy densities of cathode materials, EVs currently only have a small fraction (~1%) of the worldwide vehicle market [3,4]. Among the commercialized cathode materials ($LiCoO_2$, $LiNi_xMn_yCo_zO_2$ and $LiFePO_4$, *etc.*), the amount of cyclable Li^+ is, in principal, restricted by the reversible redox couple of transition metals (TM) in the cathode, and the charge compensation by anion redox couples will result in significant stability issues [5–8]. Nevertheless, in recent research, anion redox reactions have been found to be partial reversible in Li-rich environments [7,9–11]. In layered lithium-rich transition-metal oxides (LLO) with the general formula $xLi_2MnO_3{\cdot}(1\text{-}x)LiMO_2$ (M = Mn, Ni, Co, *etc.*) or $Li_{1+x}Ni_yCo_zMn_{1\text{-}x\text{-}y\text{-}z}O_2$, both irreversible and reversible oxygen redox reactions were observed [12–15]. Compared with traditional layered oxides ($LiMO_2$), the crystal structure of LLO is more stable with oxygen ions participating in charge compensation, bringing a much improved cyclic stability at high states of delithiation [15–18]. Calculations suggest that this improvement stems from the unique electronic structure in the Li-rich environment of LLO: the Li–O–Li configuration in LLO promotes the formation of an unhybridized O 2p state located above the hybridized O 2p state and thus is more easily oxidized [19]. However, though the reversible anion

* Corresponding author.
** Corresponding author.
*** Corresponding author.
E-mail addresses: lzhen@hit.edu.cn (L. Zhen), gzcao@u.washington.edu (G. Cao), cy_xu@hit.edu.cn (C.-Y. Xu).
[1] These authors contributed equally to this work.

https://doi.org/10.1016/j.nanoen.2020.104644
Received 9 January 2020; Received in revised form 13 February 2020; Accepted 21 February 2020
Available online 24 February 2020

redox reaction is attractive for boosting the energy density of LIBs, the accompanied irreversible oxygen evolution seems to be inevitable [20,21], resulting in critical problems including the poor cycling performance and voltage decay that hinder the practical application of LLO.

In principle, the oxygen redox reaction follows a sequence of electro hole→peroxo-like O–O dimers→O_2 release during the delithiation [21,22]. Seo et al. [19] claimed that once oxygen participates in charge compensation, the oxidized oxygen ions in the Li-rich environment are more likely to be rotated and thus tend to form peroxo-like O–O dimers. However, peroxo-like O–O dimers have only been experimentally verified in Li_2MO_3 when M represents 4*d* or 5*d* transition metal ions [23,24], and solid evidence of the peroxo-like O–O dimer formation has not yet been found in LLO. This phenomenon could be interpreted by the reductive coupling mechanism of 4d or 5d transition metal ions with high covalency M-O bonds, which thermodynamically stabilize the peroxo-like O–O dimers and suppress subsequent O_2 release [21,24,25]. Unfortunately, for all earth-abundant elements, the M-O covalency is insufficient to have such a strong reductive coupling [21,26]. Despite the initial promise, there has been little progress on suppressing the irreversible oxygen redox reaction in LLO.

In this work, the irreversible oxygen release in LLO was successfully suppressed by introducing surface defects, which were created by changing the local chemical compositions and increasing the concentration of oxygen vacancies. The modified LLO exhibits excellent cycling stability with a capacity retention of 94.5% at 0.5C after 100 cycles; moreover, no redox reaction below 3.0 V was detected after long-term cycling, indicating a suppressed phase transition from LLO to spinel. The enhanced reversibility of the oxygen redox reaction was verified by *ex-situ* X-ray photoelectron spectroscopy (XPS) analysis. Furthermore, DFT calculations revealed that the charge transfer between O ions was alleviated by oxygen vacancies, strengthening the covalency between Mn and O–O dimers. Charge transfer between Mn cations and O–O dimers, which can be described as a reductive coupling effect,[7] is considered to thermodynamically inhibit the irreversible oxygen release.

2. Experimental

2.1. Synthesis of LLO with defective surface layer

Lithium hydroxide monohydrate ($LiOH{\cdot}H_2O$), manganese sulfate monohydrate ($MnSO_4{\cdot}H_2O$) and nickel sulfate hexahydrate ($NiSO_4{\cdot}6H_2O$) were used as Li, Mn, Ni sources, respectively. Sodium carbonate (Na_2CO_3) and sodium sulfide nonahydrate ($Na_2S{\cdot}9H_2O$) were used as precipitants. All the chemicals were analytical reagents, purchased from Sigma-Aldrich, and used without purification. 1 g Na_2CO_3 and 2 g $Na_2S{\cdot}9H_2O$ were dissolved in the mixture of 10 mL ethanol and 20 mL deionized water to form solution A, 6 mmol $MnSO_4{\cdot}H_2O$ and 2 mmol $NiSO_4{\cdot}6H_2O$ were dissolved in 10 mL deionized water to form solution B. Both solutions were stirred for 1 h until transparency was achieved, then solution B was added into solution A dropwise under continuous stirring. The resulting solution was stirred for another 1 h, and black precipitates were collected by solvent evaporation at 80 °C. The dried powders were mixed with $LiOH{\cdot}H_2O$ with a molar ratio of Li: M (M = Mn + Ni) = 8:1, and were heated to 500 °C for 2h first, and then to 900 °C for 12 h with a ramping rate of 3.5 °C/min. The products were washed with deionized water and ethanol several times to remove residual Li^+, Na^+, $SO_4^{2-}$and S^{2-}, and finally dried in an oven at 60 °C for 4 h. The resulting LLO was labeled as LLO-DS.

To identify the role of Na_2S in the reaction, LLO was synthesized through traditional co-precipitation method without the addition of Na_2S during the mixture of MCO_3 (M = Mn, Ni) precursors with $LiOH{\cdot}H_2O$. To obtain MCO_3 precursor, 1 g Na_2CO_3 was dissolved in the mixture of 10 ml ethanol and 20 mL deionized water to form solution A, 6 mmol $MnSO_4{\cdot}4H_2O$ and 2 mmol $NiSO_4{\cdot}4H_2O$ were dissolved in 10 ml deionized water to form solution B. The two solutions were stirred for 1 h until the mixture became transparent, then solution A was added into solution B drop by drop under continuous stirring, and the obtained solution was kept stirring for 1h. The product was washed with deionized water and ethanol several times to remove the residual Na^+ and SO_4^{2-} and dried at 80 °C.

The precursors mixed with $LiOH{\cdot}H_2O$ with a molar ratio of Li: M (M = Mn + Ni) = 1.65:1 were calcined in the same manner as described for LLO-DS. The products were washed with deionized water and ethanol several times to remove residual Li^+, and finally dried in an oven at 60 °C for 4 h. The resulting LLO sample were labeled LLO-CO. The concentration of transition metal ions in the precursor of LLO-DS and LLO-CO was 2.55 and 7.34 mmol g^{-1} base on the ICP measurements. To eliminate the influence of excessive Li content in LLO-DS, the precursor of LLO-CO was mixed with $LiOH{\cdot}H_2O$ with a molar ratio of Li: M (M = Mn + Ni) = 8:1, the obtained powders were washed and labeled as LLO-LR.

2.2. Materials characterization

The morphology and particle size of samples were characterized by scanning electron microscope (SEM, FEI Sirion XL30) and transmission electron microscope (FEI Tecnai G^2 F20). Thermogravimetric analysis (TGA) was performed on a TG instrument (Q50 TGA) with a ramping rate of 5 °C/min in air. X-ray diffraction (XRD) patterns were recorded on a Rigaku-Dmax 2500 diffractometer using Cu K_α radiation (λ = 0.15406 nm, 40 kV, 40 mA). The Rietveld refinements were carried out by the software package GSAS with the EXPGUI interface. The lattice constants, atomic positions, phase constituents, size distribution, atomic occupancies were refined. The anisotropic line broadening was modeled by six strain parameters, which takes into account the anisotropic strain broadening of hexagonal symmetry [16]. Li^+/Ni^{2+} interlayer mixing along (001) crystallographic direction was taken into account in trigonal $R\bar{3}m$ space group, the exchanged Li, Ni atoms were set in the same position with a total occupancy of 1. The refined lattice parameters were simplified by the $R\bar{3}m$ phase with higher symmetry. High temperature *in-situ* XRD patterns were collected on a Rigaku-Dmax 2500 diffractometer equipped with heating module in air with a ramping rate of 5 °C/min and scanning rate of 8°/min. The data was collected every 25 °C from 300–600 °C.

Z-contrast imaging and electron energy loss spectroscopy (EELS) measurements were performed on a double aberration-corrected S/TEM (FEI Titan Cubed G^2 60–300) operated at 300 kV to analysis the crystal structure at atomic scale. The intensity in high angle annular dark field scanning transmission electron microscopy (HADDF-STEM) images reflected the average atomic number of each atomic column (~$Z^{1.5}$ to $Z^{1.8}$). The *ex-situ* TEM samples were obtained by dissembling cycled cells inside an Ar-filled glovebox, the cycled electrodes were first immersed in dimethyl carbonate (DMC) for 24 h and then washed with DMC 5 times. Samples were stored inside sealed Al bags before being transferred into the TEM chamber.

Inductively coupled plasma atomic emission spectroscopy (ICP-AES) analysis carried out on inductively coupled plasma–optical emission spectrophotometer (PerkinElmer Optima 8300) was performed to identify the chemical composition. The specimens were completely dissolved in aqua regia under continuous stirring, and the obtained concentration is 10 mg L^{-1}. X-ray photoelectron spectroscopy (XPS) measurements were done on a Thermo Fisher Scientific VG Kα Probe spectrometer. For the Ar etched samples, the minimum etch time was 30 s and the etch voltage was 500 V, thus the etching rate was estimated to be 5.4 nm min^{-1}. To facilitate the etching, all samples were cast into electrodes. Samples for the *ex-situ* XPS measurements were dissembled in an Ar-filled glovebox immediately at the set voltages. The cycled electrodes were first immersed in dimethyl carbonate (DMC) for 24 h and then washed by DMC for 5 times. The treated electrodes were transferred to the XPS chamber with the protection of homemade

protectors to avoid oxidation. To eliminate the shielding effect of the solid electrolyte interphase (SEI), all cycled electrodes were etched by Ar for 30 s with an etch voltage of 500 V. The resulting patterns were calibrated based on the hydrocarbon C 1s line located at 284.6 eV. For the *ex-situ* XPS results, to ensure the reliability of XPS analysis, the line shapes were fixed with a Lorentzian/Gaussian (L/G) ratio of 20%, the full width at half maximum (FWHM) of each peak were restricted between 1.2 and 1.6. Considering the complexity of the O 1s peak, each pattern was fitted with both three and four peaks, and the most reasonable fit with a minimum number of components were chosen for further analysis. The error bars shown in Fig. 4c were calculated to estimate the uncertainty of O^-. The method of Ref. 2 was utilized for the uncycled samples to determine the XPS detect limitation of O^- [27]. The elemental composition on the surface was calculated on the basis of Scofield's relative sensitivity factors.

2.3. Electrochemical measurements

The cathodes were made by mixing 75 wt% as-prepared samples, 15 wt% Super P conductive carbon and 10 wt% poly(vinylidene fluoride) (PVDF) in N-methyl-2 pyrrolidone (NMP). The slurry was spread onto an aluminum foil and dried in a vacuum oven at 120 °C for 10h. The electrochemical measurements were carried out using a CR2016 coin-type cells with a Celgard 2400 membrane as a separator. Lithium foils were used as the counter and reference electrodes. The electrolyte was composed of 1 M $LiPF_6$ solution in ethylene carbonate (EC)/dimethyl carbonate (DMC) mixture solution (1:1 by volume). Galvanostatic charge/discharge cycle tests were carried out on Land CT2001A battery test systems (LAND Wuhan Corp., China) with a potential range from 2 to 4.8 V at room temperature. Cyclic voltammetry (CV) and the electrochemical impedance spectroscopy (EIS) measurements were performed on an electrochemical workstation (CHI 660C) (Shanghai Chenhua Instrument Corp., China). The CV data was collected with a two-electrode coin cell assembly at a rate of 0.05 mV/s at room temperature; EIS was examined by applying an AC voltage of 5 mV over the frequency range of 0.01 Hz to 100 kHz.

2.4. Computation methods

Density functional theory (DFT) calculations were carried out with the Vienna *ab* initio simulation package [28]. The Projector Augmented Wave (PAW) framework was used to describe the core electrons [29]. Generalized gradient approximation (GGA) with a Hubbard U correction following the rotationally invariant form was employed to evaluated the electron exchange-correlation energy [30]. Effective U values for Ni and Mn of 6.0 and 3.9 eV were adopted from previous work [31,32]. The energy cut-off of the plane wave basis set was set at 520 eV. The initial configuration of $Li_{1.2}Ni_{0.2}Mn_{0.6}O_2$ studied in this work, which contained 120 atoms, was adopted from the theoretical work done in Zhou's group [20]. The Monkhorst-Pack method with a k-points mesh of $2 \times 4 \times 2$ was used to sample the Brillouin-zone. Each structural optimization fully relaxed the cell parameters and atomic positions until the force per atom in the supercell was less than 0.01 eV/Å. In order to achieve accurately oxygen redox states, the Heyd-Scuesria-Ernaerhof (HSE06) hybrid functional was used to obtain density of states and the charge density of the LLO materials [33].

Oxygen vacancies were created in $Li_{1.2}Ni_{0.2}Mn_{0.6}O_2$ to identify the role of vacancies upon delithiation. Based on the various surrounding environments, 60 oxygen atoms in a supercell of $Li_{1.2}Ni_{0.2}Mn_{0.6}O_2$ were divided into 5 types: oxygen coordinated by 3 Mn and 3 Li; 2 Mn,1 Ni and 3 Li; 1 Mn and 5 Li; 1 Ni and 5 Li; 1 Mn, 1 Ni and 4 Li. Each oxygen site was examined to find the lowest energy configuration. One vacancy in the cell corresponds to a vacancy concentration of 1.67 at%. The formation energy of the oxygen vacancy (E_F) was calculated with the following equation:

$$E_F = E(Li_xM_yO_{2-\alpha}) + \alpha/2E(O_2) - E(Li_xM_yO_2) \quad (1)$$

where α is the concentration of oxygen vacancies, $E(Li_xM_yO_{2-\alpha})$[fx] is the calculated energy of the structure after the formation of an oxygen vacancy, $E(O_2)$ is the energy of the O_2 molecule, $E(Li_xM_yO_2)$ is the calculated energy of the structure before formation of the oxygen vacancy. The energy of O_2 molecule is corrected according to previous research [34].

Li/Ni anti-site defects were also been considered in this investigation. Each of 8 Li atoms within distance of 3.8 Å of Ni were considered to find the most likely structure; the Li/Ni exchange percentage is 16.67 at %. For the charging process, we used the basin-hopping algorithm to search for the global minimum configurations of several delithiated states of $Li_xNi_{0.2}Mn_{0.6}O_2$ ($x = 0.6, 0.5, 0.4$). 80 various Li-vacancy arrangements were tested in each delithiated state.

3. Results and discussion

3.1. Characterization of LLO with defective surface layer

Two types of precipitants, namely CO_3^{2-} and S^{2-}, were utilized to initiate oxygen vacancies, forming a defective surface layer on LLO particles (denoted as LLO-DS); the other group of samples using only CO_3^{2-} as a precipitant (denoted as LLO-CO) was also prepared, aiming to elucidate the role of S^{2-}. The phase compositions and crystal structures of LLO-CO and LLO-DS were investigated through X-ray diffraction (XRD) with Rietveld refinements (Fig. 1a and Fig. S1a). Both samples have the same phase composition as the Li-rich layered structure (Fig. 1b) and similar lattice parameters, with the exception of reduced Li^+/Ni^{2+} interlayer mixing along the (001) direction in LLO-DS (Table S1). Scanning electron microscope (SEM) image of LLO-DS (Fig. 1c) shows an octahedral morphology and a particle size of 200–500 nm, while LLO has microsphere morphology (Fig. S1b). A layer with brighter contrast was found to be uniformly distributed on the surface of particle in the bright-field transmission electron microscope (TEM) image of LLO-DS (Fig. 1d), and the high-resolution TEM image in Fig. 1e shows the amorphous nature of that layer with thicknesses of several nanometers.

The chemical compositions of LLO-DS and LLO-CO were determined by inductively coupled plasma emission spectroscopy (ICP-AES) (Table S2). No signal for Na nor S were detected in either of the two samples, and the slightly higher Li content in LLO-DS is probably associated with the high Li content in the surface layer. The surface element distribution of LLO-DS particles was determined through an EDS line scan under scanning transmission electron microscope (STEM) mode (Fig. 1f and g). Affected by the octahedral shape, the content of Mn and O decrease from the core area to the surface. It should be noted that this content decreases substantially at the outermost surface (Region 1), which can be ascribed to a nonlinearity in the change in thickness at the outermost surface and a decreased content of Mn and O in the surface layer. The content of Ni reduces slowly in Region 2, but increases in Region 1, indicating a higher Ni content in the surface layer.

X-ray photoelectron spectroscopy was employed to confirm the chemical compositions and the oxidation states of the near surface of LLO-DS and LLO-CO. The calculated relative content of metal elements (Table S3) indicates higher Li and Ni content at the surface of LLO-DS, in accordance with the ICP and EDS analyses. High-resolution XPS spectra of Mn, Ni and O were fit (Fig. S2); the ratios of peak areas are summarized in Table S4. Compared with LLO-CO, LLO-DS has a higher Ni oxidation state and lower Mn oxidation state on the surface (a lower percentage of Ni^{2+} and Mn^{4+}). As seen from the O 1s spectra, the peak in 531–532 eV with lower electron density (O_{led}) than that of fully-coordinated O^{2-} in the lattice (O_{lat}, located in 529–530 eV) can be assigned to either surface absorbed O or oxygen adjacent to oxygen vacancies [35–37]. To verify this speculation, the precursor of LLO-DS

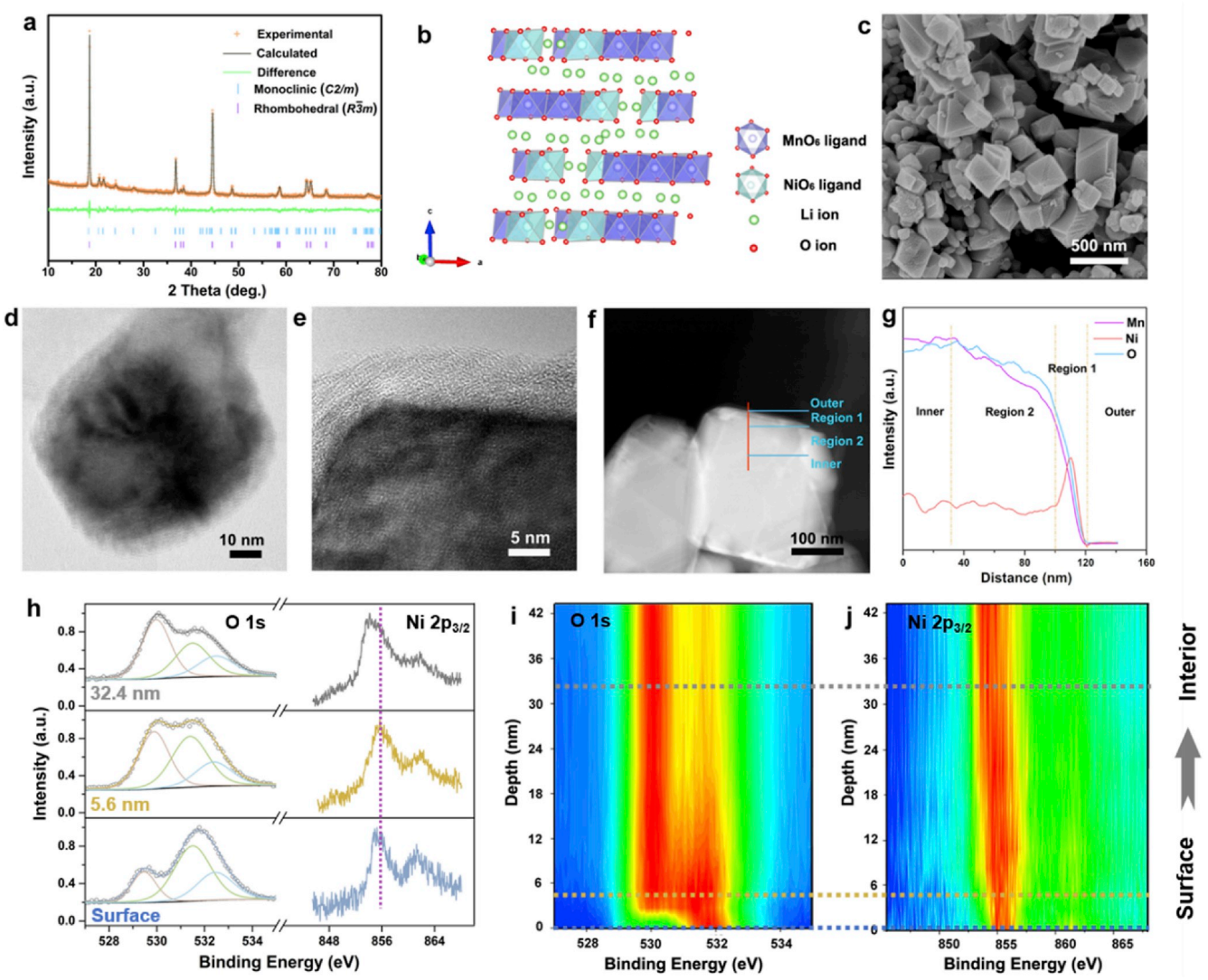

Fig. 1. Phase and chemical compositions of LLO with a defective surface layer. (a) Rietveld refinement of XRD patterns of LLO-DS. The refinements were performed with: *C2/m* space group (blue vertical tick marks) and trigonal $R\bar{3}m$ space group (purple vertical tick marks). (b) Crystal structure of $Li_{1.2}Ni_{0.2}Mn_{0.6}O_2$. The structure was adopted from the theoretical work of Zhou's group [20]. (c–e) SEM image (c) and TEM images (d and e) of LLO-DS. (f, g) EDS line scan on an individual particle (f) and the corresponded elemental distribution of Mn, Ni, O elements (g). The red line in (f) presented the scan area, and four regions were divided. Except for the outer and inner regions, Region 1 is the outmost region, which is dominated by the surface layer; Region 2 is the near core region, which is dominated by the bulk materials. (h–j) O 1s and Ni $2p_{3/2}$ spectra (h) of LLO-DS at depth of 0, 5.6 and 32.4 nm (corresponding to the dashed line in (i) and (j)), XPS depth-profile of O 1s (i) and Ni $2p_{3/2}$ (j) spectra.

was calcined in an oxygen atmosphere (denoted as LLO-DS-O), and then the valence state of oxygen on the surface of LLO-DS-O was compared with that in LLO-DS. The O 1s peak of LLO-DS-O (Fig. S3) has a lower proportion of O_{led} (61.1%) as compared with that of LLO-DS (70.9%), indicating the O_{led} peak in LLO-DS is not dominated by absorbed O. Thus, we conclude that oxygen vacancies, namely uncoordinated X–O (X = Mn, Ni or Li) bonds, are abundant in the surface layer of LLO-DS. Depth-profiling O 1s spectra of LLO-DS (Fig. 1h and i) shows that the percentage of O_{led} is continuously reduced from the surface to the interior, while the O 1s peak of LLO-CO changes little except for the outmost area (Figs. S4a and b). The peak position of the Ni $2p_{3/2}$ spectra remains unchanged until the etching depth reaches 20 nm (Fig. 1h and j), and Ni in the interior region (>20 nm from the surface) has a lower valence state (lower binding energy). Therefore, it is likely that the surface layer on LLO-DS is a non-stoichiometric oxide with substantial oxygen vacancies and a higher ratio of Ni and Li as compared to LLO-CO.

It is worth mentioning that the thickness of the surface layer in LLO-DS is estimated to be only 5–10 nm from TEM images (Fig. 1d and e), but the valence change of O and Ni extends deeper into the material. Except for deviations caused by varying etching rates at different depths, such difference should reflect a continuous valence change at the interface between the bulk material and the surface layer. The atomic structure near the surface of LLO-DS was investigated with high-angle annular dark-field (HADDF) scanning transmission electron microscope (Fig. 2a). The specific Li-TM ordering in LLO with dumbbell-like dots was seen inside the particle, while the outmost area with a thickness of 5 nm showed amorphous features. In addition, two projections along <100> and <110> zone axes of the *C2/m* structure with different atom stackings (Fig. 2b) were observed in the particle, suggesting the existence of stacking faults [38], which is evidenced by the diffuse streaks in FFT pattern (inset of Fig. 2a). At the interface between the ordered bulk material and amorphous surface layer (Fig. 2c), the typical Li-rich layered structure with ordered TM-TM dumbbells gradually turns into a continuous dotted pattern, indicating the existence of cation mixing at the interphase [39]. Such atomic configuration change showed the co-occupancy of Li and transition metals in the octahedral sites at the

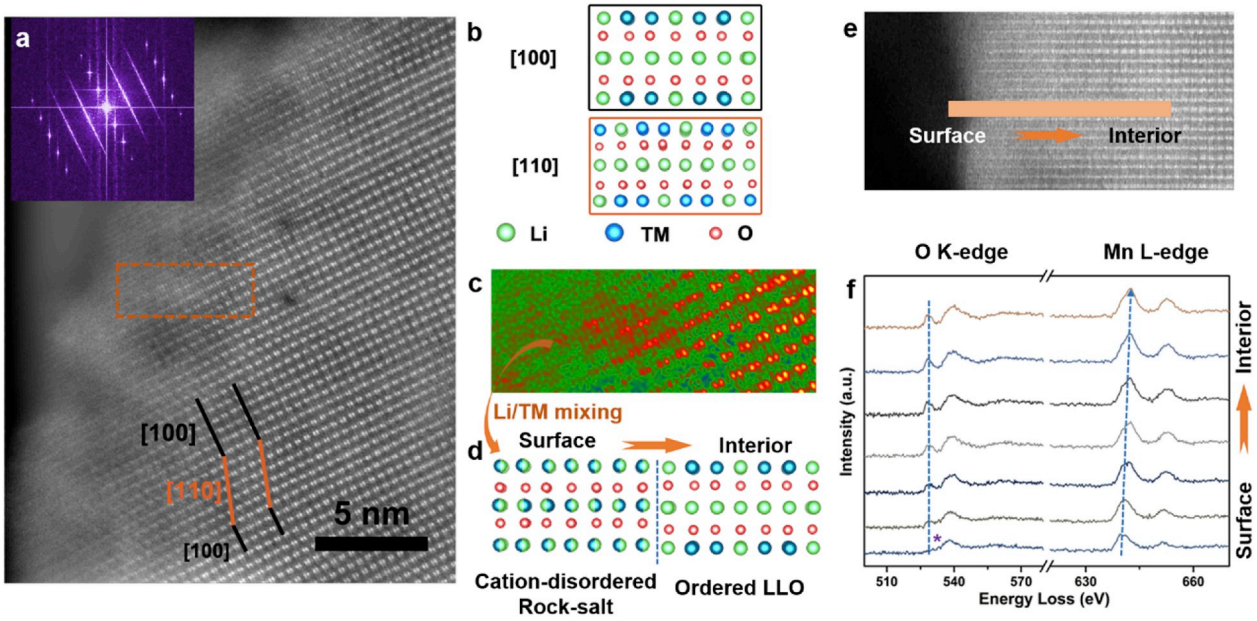

Fig. 2. Atomic structure and chemical states of LLO with a defective surface layer. (a) High-angle annular dark-field (HAADF)-STEM image of LLO-DS. The corresponded FFT pattern is shown as inset, in which the continuous spots are indicative of planar defects. The area marked by dark and orange parallel lines show two projections along <100> and <110> zone axes of *C2/m* structure, respectively. (b) Atomic models of the monoclinic structure along <100> and <110> directions. Atoms are distinguished by different colors. (c–d) High-magnification image (c) of the selected area in the orange dash square in (A), and schematic diagram (d) of the co-existence of cation-disordered rock-salt phase and LLO phase revealed in (c). the atomic models are shown with the same colors in (c). (e–f) HAADF-STEM image (e) showing the area from the surface to interior in a single particle of LLO-DS, The O K-edge and Mn L-edge electron energy loss spectroscopy (EELS) spectra (f) from the surface to the interior area obtained from the dark pink line in (e). The purple asterisk marks the position of the shoulder peak in the O K-edge spectra. The blue arrow indicates the orientation of the spectra.

interphase area, which could be referred to a cation-disordered rock-salt phase (Fig. 2d) [37]. For the LLO-CO, the HAADF/STEM image (Fig. S5) revealed the layered feature and the surface of LLO-CO is clean without amorphous layer. O K-edge and Mn L-edge electron energy loss spectroscopy (EELS) spectra (Fig. 2f) from the surface to the interior of LLO-DS (Fig. 2e) were recorded to investigate the evolution of the chemical states. The intensity of the pre-edge peak (~528 eV) in the O K-edge spectra increased gradually from the surface to the interior; and a weak shoulder peak (~530 eV), marked with an asterisk, was observed near the surface. It is well-known that the pre-edge of the O K-edge spectra reflects transition of electrons from the O 1s orbital to unoccupied 2p orbital that hybridized with TM ions [40,41], the reduced pre-edge and split shoulder peak at higher energy are therefore indicative of the higher content of uncoordinated TM-O bonds, suggesting the present of oxygen vacancies in the surface layer that is in accordance with the XPS analysis. The Mn L-edge spectra show a chemical shift of 2.5 eV from the surface to the interior, indicating a lower valence of Mn on the surface [42,43].

We have shown that the surface layer in LLO-DS is non-stoichiometric with considerable oxygen vacancies, however, the role of co-precipitants on the formation of this layer is still not clear. Thermogravimetric (TG) curves of the precursors of LLO-CO and LLO-DS (Fig. S6) revealed different weight loss procedures for each sample, suggesting different phase transition routes during calcination. High temperature *in-situ* XRD patterns were then collected to identify the different reaction routes. For LLO-CO, the carbonates gradually decomposed from 300 to 500 °C and the reflections of $Li_{1.2}Ni_{0.2}Mn_{0.6}O_2$ appeared at 325 °C (Fig. S7), suggesting that the reaction is accompanied by a consuming of carbonates. Both carbonates and sulfides of the transition metals were detected in the precursor of LLO-DS (Fig. S8), and the relative intensity of peaks in reference to LLO was quite low before being heated to 500 °C, suggesting that the phase transition of TM sulfides is more difficult than that of TM carbonates. Moreover, a mixture of LLO, spinel and rock salt phases were observed when only S^{2-} served as the precipitant (Fig. S9), implying that an inhomogeneous cation distribution and substantial cation mixing is introduced during the reaction base on TM sulfides. We therefore deduce that the formation of the surface layer probably attributed to the simultaneously oxidation of S^{2-} during the reaction which prevents the ordered close-packing of anions and cations.

3.2. Electrochemical properties of LLO with defective surface layer

The electrochemical properties of LLO-DS and LLO-CO were evaluated in Li-metal half cells with potentials between 2.0 and 4.8 V at 0.5C (1C = 200 mA g^{-1}). Both samples showed charge capacity around 280 mA h g^{-1} in the initial cycle, suggesting the comparable delithiated states; and the higher initial capacity of LLO-CO is likely due to the higher content of Mn^{2+} formed after irreversible oxygen release. A comparison of the voltage profiles of LLO-DS (Fig. 3a) and LLO-CO (Fig. S10a) shows a higher plateau of the oxygen redox reaction in LLO-DS (4.74–4.80 V) than that in LLO-CO (4.56–4.80 V), indicating that a higher driving force is needed for the oxygen redox reaction in LLO-DS in the first cycle. The high oxygen redox plateau in LLO-DS can be attributed to either a large polarization or a dynamically/thermodynamically suppressed oxygen evolution in LLO-DS. The potential of the Ni^{4+}/Ni^{2+} redox reaction in LLO-DS during the first discharge process (3.86 V) is slightly higher than that of LLO-CO (3.80 V), as seen from the derivative curves (Fig. 3b); thus, the higher oxygen redox plateau is more likely due to a dynamically/thermodynamically restriction rather than polarization.

Long-term cycling tests of LLO-DS and LLO-CO were performed at 0.5 and 1C (Fig. 3c and Fig. S10b). Although the initial discharge capacity of LLO-CO is higher, LLO-DS showed an improved cycling stability. The discharge capacities of LLO-DS are 173 and 158 mA h g^{-1} after 100 cycles at 0.5 and 1C, corresponding to 94.5% and 91.3% capacity retention, respectively. For LLO-CO, after the same number of cycles, the discharge capacities are 134 and 119 mA h g^{-1} at 0.5 and 1C,

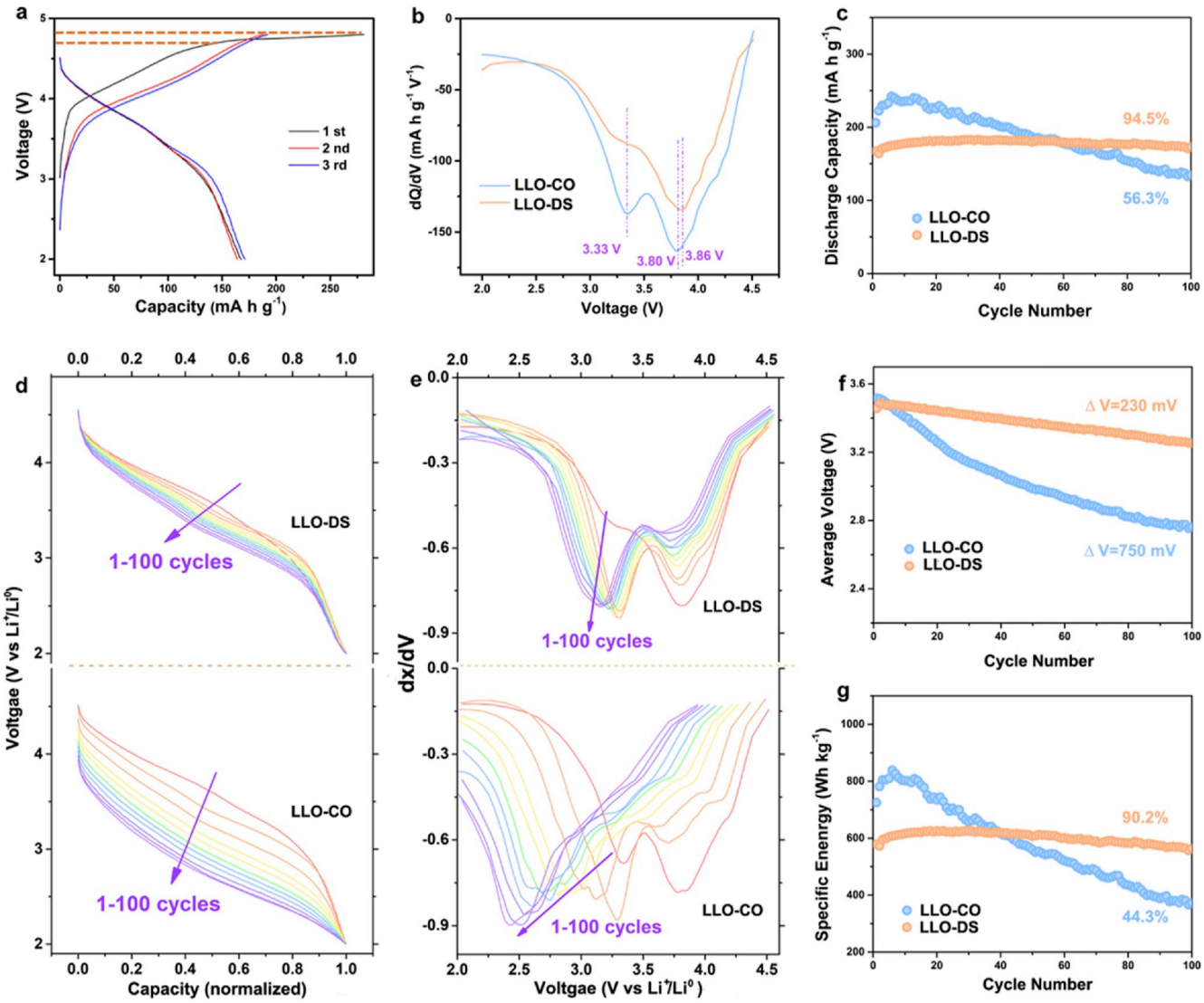

Fig. 3. Electrochemical performance of LLO-DS and LLO-CO. (a, b) First three cycles charge-discharge profiles (a) of LLO-DS between 2.0 and 4.8 V with current density of 0.5C and differential capacity curves (b) of the first discharge process in LLO-DS and LLO-CO under 0.5C. (c–e) Cyclic retention of LLO-DS and LLO-CO as a function of cycles at 0.5C (c), the normalized galvanostatic discharge profiles (d) at 0.5C from 1 to 100 cycles and corresponding differential capacity curves (e) of LLO-DS and LLO-CO. The curves are plotted every 10 cycles. (f–g) Retention of the average discharge voltage (f) and specific energy density (g) in the first 100 cycles for LLO-DS and LLO-CO when cycled at 0.5C; the energy density is calculated by integrating the discharge curves and the average discharge voltage is obtained by differentiating the discharge curves.

corresponding to a capacity retention of 56.3% and 64.0%, respectively. As it has been widely accepted that the stability of LLO is primarily restricted by an irreversible phase transition upon cycling [44], the difference in stability signifies that the defective surface layer in LLO-DS has effectively enhanced the structural stability of LLO.

Another indicator of the irreversible phase transition in LLO is the shift of redox reaction potential, which could be raised by both a layer to spinel phase transition and from an accumulated polarization [45]. To identify the influence of surface defects on the redox behavior in the two electrodes, the normalized discharge curves of LLO-DS and LLO-CO between the 1st and 100th cycles (Fig. 3d) was compared, and the derivative plots of each cycle (Fig. 3e) were calculated to eliminate the influence of accumulated polarization. The discharge voltage is well conserved in LLO-DS (Fig. 3d), suggesting less phase transformation and polarization in LLO-DS than in LLO-CO. In the corresponding derivative plots (Fig. 3e), the redox potential of Mn^{3+}/Mn^{4+} (~3.3 V) moved slightly towards lower potentials after 100 cycles, and the redox reaction peaks remained higher than 3.0 V after 100 cycles. Compared with the continuous damping of the high (3.3 V) to low potential peaks (2.4 V) in Fig. 3e, which are generally considered to stem from an increased spinel phase content, the suppressed voltage decay implies that the layered to spinel phase transition has been effectively suppressed in LLO-DS. Such results are further verified by the *ex-situ* XRD patterns of the cycled electrodes (Fig. S11), from which the cycled LLO-CO showed much more spinel phase as compared with the cycled LLO-DS sample. The average discharge voltage decay in the first 100 cycles is 0.23 V for LLO-DS and 0.75 V for LLO-CO, and the energy density retention in the first 100 cycles of LLO-DS is 90.2%, as compared to 44.3% for LLO-CO (. 3g). This improvement confirms the mitigated irreversible phase transitions (oxygen release and layer to spinel phase transition) and stabilized crystal structure in LLO-DS.

Considering the fact that the Li content in LLO-DS is slightly higher than that in LLO-CO (Table S2); to eliminate the probable influence of the Li content on the electrochemical performance, samples with excessive Li content (LLO-LR) was synthesized by mixing the precursor of LLO-CO with the same Li: TM ratio of LLO-DS (see details in Experimental section). The obtained pure-phase LLO-LR with "Li-rich" chemical compositions (Table S2) showed low discharge capacity (<75 mA h

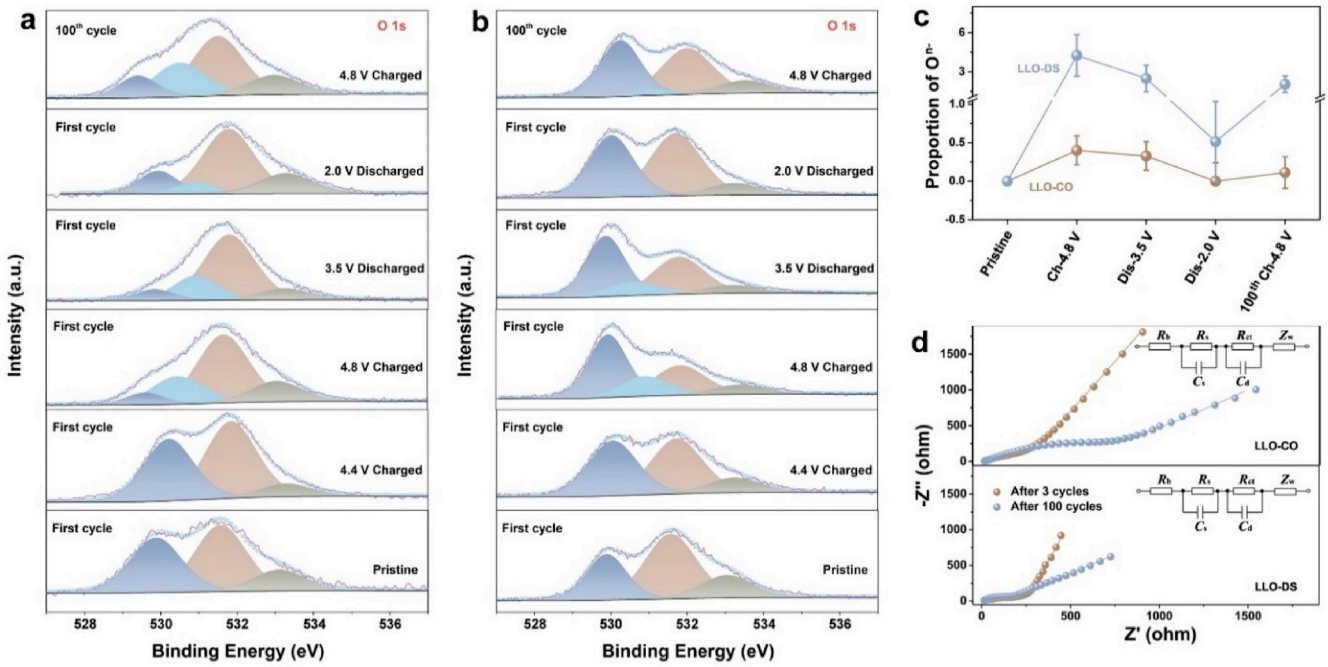

Fig. 4. Change in anionic oxidation states and electrochemical impedance of LLO-DS and LLO-CO upon cycling. (a, b) O 1s spectra of LLO-DS (a) and LLO-CO (b) at different charge states upon cycling. All the cycled electrodes are etched by Ar to eliminate the influence of surface spices. Four oxidation states of O are considered: crystal lattice O^{2-} (529.5–530.0 eV); peroxo-like O–O pairs or oxygen with localized electron holes O^{n-} (~530.5 eV); deposited oxygenated species (531–532 eV); and electrolyte oxidation (533–534 eV). Details of the analysis method are in the Experimental Section. (c) Ratio of the area of the peaks corresponding to O^{n-} and lattice O^{2-} at each stage in (a and b). (d) Impedance spectra of LLO-DS and LLO-CO collected after 3 and 100 cycles in the discharged state.

g^{-1}) and rapid capacity fading (67.6% remained after 100 cycles) under 0.5C (Fig. S12), which is probably associated with the structure collapsing after Li extracted from the Li-rich configuration during the first charge process. In consequence, the suppressed capacity fading and well reserved crystal structure in LLO-DS should not been traced from the higher Li content, but more likely to be influenced by the defective surface layer with higher Li content than interior area.

3.3. Charge compensation mechanism of LLO with defective surface layer

To unravel the anion redox process in LLO-DS and LLO-CO, *ex-situ* XPS measurements upon cycling were carried out; the results are shown in Fig. 4a and b. To eliminate the shielding effect of the solid electrolyte interphase (SEI), all cycled electrodes were etched by Ar for 30 s with an etch voltage of 500 V. For the LLO-DS samples (Fig. 4a), the O 1s spectra barely changes when the electrode is charged to 4.4 V, showing that no significant oxygen redox reaction occurs at this voltage in the first cycle. However, when fully charged (4.8 V), an additional peak centered at 530.5 eV corresponding to O^{n-} ($n < 2$) with a lower electronic density than crystallized O^{2-} (~529.5 eV) emerged, implying that partially oxidized O^{2-} species remain in the crystal of electrode materials [46]. The reduced intensity of the O^{n-} peak in the following discharge cycles indicated a reduction of O^{n-}. It is worth mentioning that a small portion of the O^{n-} peak remains when the electrode is discharged to 2.0 V, which is probably due to either a deviation caused by a relatively weak crystalized O^{2-} peak or charge transfer between O^{n-} with uncoordinated M-O bond in the surface layer. After 100 cycles, a large proportion of the O^{n-} characteristic peak is detected in the fully charged LLO-DS, indicating a highly reversible oxygen redox reaction. A similar trend for the anion redox reaction in the first cycle was detected in LLO-CO, however, the characteristic O^{n-} peak is negligible after 100 cycles, suggesting a much lower reversibility of the anion redox in LLO-CO as compared to LLO-DS.

The ratio of the peak areas corresponding to the O^{n-} and lattice O^{2-} species at each stage (Fig. 4c) were derived from the XPS spectra to compare the reversibility of anion redox reaction in the two samples. An estimation of the uncertainties caused by overlapping peaks is indicated by the error bars. These results show that, in the surface area detected by XPS, the proportion of O^{n-} in the 4.8 V charged samples remains at 48.2% in LLO-DS after 100 cycles, suggesting much improved reversibility of anion redox reaction in LLO-DS. Noted that the fraction of O^{n-} is much higher in LLO-DS, which is unusual as over-oxidation should facilitate rotation of O^{n-} ions to form O–O bond, resulting in irreversible release of O_2 and a structural distortion. Therefore, we deduce that the defective surface layer in LLO-DS suppresses irreversible oxygen release from the material and thereby facilitates the reversible anion redox reaction during cycling. Such a high reversible anion redox was barely revealed in Li-rich oxides with 3*d* transition metal ions, as previous research have showed that oxidized O^{n-} is thermodynamically unstable when paired with 3*d* transition metal ions [21,22]. Compared with other engineering strategies such as *in-situ* or *ex-situ* coating by a secondary phase to kinetically suppress oxygen release [47,48], the creation of defects on the surface is more likely to accommodation the bulk atomic structure and consequently manipulate the anion redox stability. As both the inactive rock-salt phase and intergranular cracks created by irreversible oxygen release will substantially lower the ionic/electronic conductivity and thus increase the electrochemical impedance of LLO [17,18], electrochemical impedance spectroscopy (EIS) was employed to explore the resistance change upon cycling (Fig. 4d). The increment of charge-transfer resistance (the semicircle curves at medium to low frequency) from the 3rd to the 100th cycle in LLO-DS is much slower than that in LLO-CO, suggesting less rock-salt phase and fewer intergranular cracks formed in LLO-DS during cycling. This is further confirmed by TEM images of the cycled samples (Fig. S13), in which the LLO-DS particles are preserved, while serious cracking is observed in LLO-CO.

DFT calculations were carried out to investigate the electronic structure and redox behavior of O in defective LLO. The crystal structures and calculated formation energy of defects (oxygen vacancy and Li/Ni mixing) are shown in Fig. S13. Oxygen vacancies are found to be energetically favorable when coordinated with 5 Li and 1 Ni ions, and

vacancies promote the formation of Li/Ni mixing (Fig. S14). At the electronic level (Fig. 5a and b), the electrostatic repulsion between oxygen vacancy and nearby Li ions (Li1) induces higher charge transfer between Li1 with the coordinated oxygen ions (O1 an O2), resulting in the lower oxidization states of O1 and O2 (increased Bader charge) in oxygen vacancy-rich $Li_{1.2}Ni_{0.2}Mn_{0.6}O_{2-x}$ and consequently higher electrostatic repulsion between O1 and O2 (Fig. 5b). Further delithiation promotes the redox reaction of oxygen ions (Fig. 5a and b), and O–O dimers preferentially formed from oxygen ions that were coordinated with a Li vacancy in the transition metal layer, when 0.8 Li per FU was extracted from the material (corresponded to an initial charge capacity of ~250 mA h g^{-1}). The O1–O2 dimer in $Li_{0.4}Ni_{0.2}Mn_{0.6}O_2$ is highly distorted, with a bond length of 1.25 Å – quite close to the experimental bond length of O_2 (1.21 Å) [49] – and thus it can be classified as a superoxide. The calculated formation energy of an oxygen vacancy on the O2 site is 0.22 eV (2.3 meV per atom), implying facile formation of oxygen vacancies. This over-oxidized oxygen ions, which is different from that described in previous computational work[20] but in accord with experimental observations [20,50], is likely associated with the Li/Ni anti-site defect that results in a weak Li–O hybridization and higher oxidization states of nearby oxygen ions. However, in the defect-rich $Li_{1.2}Ni_{0.2}Mn_{0.6}O_{2-x}$ with lower oxidization states of O1 and O2, the O1–O2 bond length in delithiated $Li_{0.4}Ni_{0.2}Mn_{0.6}O_{2-x}$ is 1.31 Å and could be classified as a peroxide species [49]. Interestingly, our Bader analyze indicates the increased charge on Mn1 and the charge compensation on O1 and O2 in $Li_{0.4}Ni_{0.2}Mn_{0.6}O_{2-x}$ is less than that in $Li_{0.4}Ni_{0.2}Mn_{0.6}O_2$, suggesting charge transfer between the O1–O2 dimer and Mn1 through what is generally considered to be a reductive coupling mechanism [21]. Such charge transfer could be understood by the less splitting of bonding band (π and σ) and antibonding band (π* and σ*) of O–O molecular orbital (Δ^{σ}_{O-O} *and* Δ^{π}_{O-O}) in the less oxidized O–O dimer, which enable the charge transfer between π* and empty metallic band of Mn^{4+} [51].

Partial density of states (PDOS) of $Li_{0.4}Ni_{0.2}Mn_{0.6}O_2$ and $Li_{0.4}Ni_{0.2}Mn_{0.6}O_{2-x}$ further confirm the reductive coupling mechanism (Fig. 5c). The O1–O2 dimer in $Li_{0.4}Ni_{0.2}Mn_{0.6}O_2$ has a higher oxidation state with partial empty π* antibonding states pushed above the Fermi level, while the π* orbital in $Li_{0.4}Ni_{0.2}Mn_{0.6}O_{2-x}$ hybridizes with the Mn 3*d* orbital to lie below the Fermi level. Considering the fact that the 2*p* molecular orbitals of $(O_2)^{2-}$ consist of fully occupied antibonding orbital: π* and two bonding orbitals: σ and π, while O_2 is consisted of half occupied π* and fully occupied σ and π [21], the O1–O2 dimer can be considered $(O_2)^{n-}$ $(n < 2)$ in $Li_{0.4}Ni_{0.2}Mn_{0.6}O_2$ and $(O_2)^{2-}$ in $Li_{0.4}Ni_{0.2}Mn_{0.6}O_{2-x}$. This picture can be understood from charge compensation caused by oxygen vacancies (Fig. 5d). The formation of an oxygen vacancy in the fully-lithiated state results in lower oxidization states of the nearby oxygen ions and therefore increases the O–O distance in the LiO_4 pentahedron ligand. Consequently, a less oxidized O–O dimer with a smaller rotation is formed to facilitate charge transfer to nearby Mn ions. It is worth mentioning that this role of oxygen vacancies would not occur for oxygen vacancies formed during the delithiation process, as the later ones tend to be formed on the TMO_6 ligands and

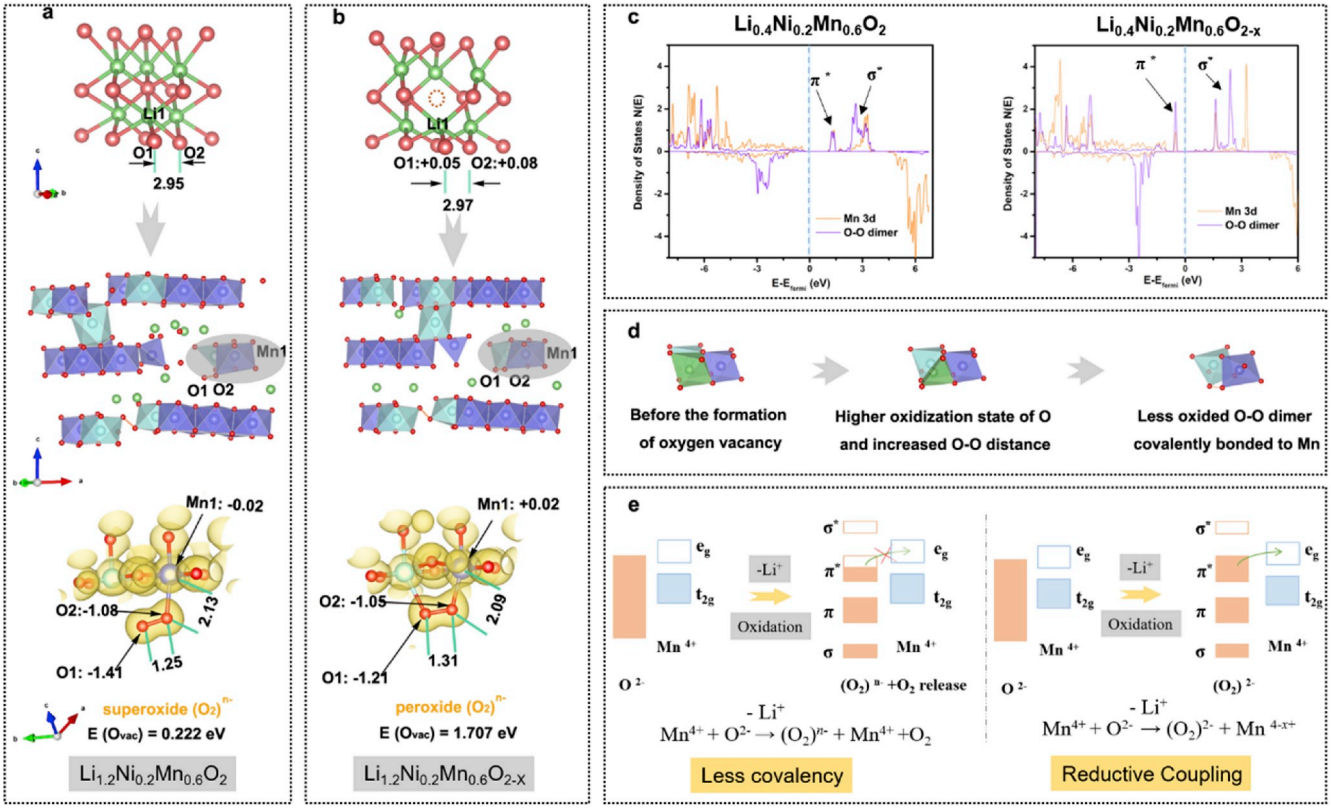

Fig. 5. DFT calculations and proposed reductive coupling stabilization mechanism in LLO-DS. (a, b) Charge transfer and change of atomic configurations when 0.8 Li per FU are extracted from $Li_{1.2}Ni_{0.2}Mn_{0.6}O_2$ (a) and oxygen vacancy-rich $Li_{1.2}Ni_{0.2}Mn_{0.6}O_{2-x}$ (b). From top to bottom: local structure of the oxygen vacancy in $Li_{1.2}Ni_{0.2}Mn_{0.6}O_{2-x}$ and corresponding region in $Li_{1.2}Ni_{0.2}Mn_{0.6}O_2$, atomic configurations when 0.8 Li per FU are extracted and isosurface of the charge density near the most unstable O–O dimers (the shadowed area in delithiated states). The oxygen vacancy is marked by dash red circles; the value of Bader charge changes (O1 and O2 after formation of oxygen vacancy in the local structure before delithiation; Mn1, O1 and O2 after delitiation in the charge density profiles) and the distance between O1–O2 and Mn1–O2 are showcased. (c) Partial density of states (PDOS) of Mn1 and the O–O dimer in $Li_{0.4}Ni_{0.2}Mn_{0.6}O_2$ (left) and $Li_{0.4}Ni_{0.2}Mn_{0.6}O_{2-x}$ (right). (d–e) Schematic diagram (d) of the enhanced Mn-(O_2) bonding in the pre-oxygen vacancy structure ($Li_{0.4}Ni_{0.2}Mn_{0.6}O_{2-x}$), and proposed charge compensation mechanism (e) in $Li_{1.2}Ni_{0.2}Mn_{0.6}O_2$ (left) and $Li_{1.2}Ni_{0.2}Mn_{0.6}O_{2-x}$ (right) showing that the less oxidized O–O dimer promotes the reductive coupling effect and thus stabilizes the structure.

therefore promote rearrangement of O and migration of transition metals, which has been demonstrated before.[42] In summary, the over-oxidation of O–O dimers to $(O_2)^{n-}$ ($n < 2$) superoxides in $Li_{1.2}Ni_{0.2}Mn_{0.6}O_2$ reduce the covalency to Mn^{4+}, therefore lead to irreversible oxygen loss, that trend will be further intensified by the Li/Ni mixing. However, the formation of oxygen vacancies in the full-lithiated state reduces the over-oxidation of O–O dimers by decreasing the oxidization states of oxygen ions, and these $(O_2)^{2-}$ species, with fully occupied π* orbitals, are covalently bonded to nearby Mn^{4+} and enhance the reductive coupling mechanism (Fig. 5e).

4. Conclusions

In summary, a highly reversible anion redox is achieved in Li-rich layered oxides by establishing a defective surface layer. The less crystallized layer was constructed by changing the chemical composition and increasing the concentration of oxygen vacancies on the surface, as characterized by HAADF-STEM, EELS and depth-profiling XPS analysis. The modified LLO material showed a substantially enhanced structural stability with 94.5% discharge capacity remained after 100 cycles, while only 56.4% remained for LLO without the surface modification. More importantly, the redox reaction potential during the discharge process is retained (>3.0 V) after long-term cycling, suggesting a suppression in the phase transition from the layered to spinel structure. *Ex*-situ XPS measurements show a higher content of oxidized O^{n-} ($n < 2$) in the modified LLO at high delithiated states. The O^{n-} remains in the modified LLO after 100 cycles, suggesting a highly reversible oxygen redox reaction. Compared with previously reported attempts at surface coating, this defect-rich surface layer not only dynamically suppresses irreversible oxygen release, but also traps O–O dimers through the reductive coupling mechanism. DFT calculations explain O–O dimer instability in LLO with Li/Ni mixing. They also show that oxidization of O–O is mitigated in LLO containing oxygen vacancies where the π* orbital has a reduced charge and is found to be covalently bonded with nearby Mn^{4+}, which enhances reductive coupling. As far as we know, this is the first time that the role of oxygen vacancies and Li/Ni mixing in the fully lithiated state of LLO has been explained in detail. Understanding the importance of the reductive coupling mechanism in Mn-based Li-rich layered structure should make it possible to achieve reversible anion redox reaction in low cost LLO materials.

Declaration of competing interest

The authors declare that they have no known competing financial interests or personal relationships that could have appeared to influence the work reported in this paper.

CRediT authorship contribution statement

Yi Pei: Conceptualization, Investigation, Writing - original draft. **Qing Chen:** Conceptualization, Investigation, Writing - original draft. **Meiyu Wang:** Investigation, Validation. **Bin Li:** Investigation. **Peng Wang:** Investigation. **Graeme Henkelman:** Writing - review & editing, Supervision. **Liang Zhen:** Conceptualization, Supervision. **Guozhong Cao:** Conceptualization, Supervision. **Cheng-Yan Xu:** Conceptualization, Writing - review & editing, Supervision.

Acknowledgements

This work was financially supported in part by National Science Foundation (CBET 1803256), National Natural Science Foundation of China (11874199) and National Basic Research Program of China (Grant No. 2015CB654901). G.H. acknowledges support from the Welch Foundation under grant F-1841. Y.P, and Q.C. would like to thank the China Scholarship Council (CSC) for supporting their study as visiting students in U.W. and UT Austin, respectively. The authors gratefully acknowledge Mrs. Xiaoyan Wang and Dr. Xiaojun Kuang from Guilin University of Technology for XRD measurements.

Appendix A. Supplementary data

Supplementary data to this article can be found online at https://doi.org/10.1016/j.nanoen.2020.104644.

References

[1] J. Lu, T. Wu, K. Amine, Nat. Energy 2 (2017) 17011.
[2] R.C. Massé, E. Uchaker, G. Cao, Sci. China Mater. 58 (2015) 715.
[3] J. Lee, D.A. Kitchaev, D.H. Kwon, C.W. Lee, J.K. Papp, Y.S. Liu, Z. Lun, R. J. Clement, T. Shi, B.D. McCloskey, J. Guo, M. Balasubramanian, G. Ceder, Nature 556 (2018) 185.
[4] Z. Xing, S. Wang, A. Yu, Z. Chen, Nano Energy 50 (2018) 229.
[5] Q. Liu, X. Su, D. Lei, Y. Qin, J. Wen, F. Guo, Y.A. Wu, Y. Rong, R. Kou, X. Xiao, F. Aguesse, J. Bareño, Y. Ren, W. Lu, Y. Li, Nat. Energy 3 (2018) 936.
[6] Q. Chen, P. Xiao, Y. Pei, Y. Song, C.-Y. Xu, L. Zhen, G. Henkelman, J. Mater. Chem. A. 5 (2017) 16722.
[7] G. Assat, J.-M. Tarascon, Nat. Energy 3 (2018) 373.
[8] Y. Pei, Q. Chen, C.-Y. Xu, H.-X. Wang, H.-T. Fang, C. Zhou, L. Zhen, G. Cao, J. Mater. Chem. A. 4 (2016) 9447.
[9] A. Manthiram, J.C. Knight, S.-T. Myung, S.-M. Oh, Y.-K. Sun, Adv. Energy Mater. 6 (2016) 1501010.
[10] N. Yabuuchi, M. Takeuchi, M. Nakayama, H. Shiiba, M. Ogawa, K. Nakayama, T. Ohta, D. Endo, T. Ozaki, T. Inamasu, K. Sato, S. Komaba, Proc. Natl. Acad. Sci. U. S. A. 112 (2015) 7650.
[11] J. Xu, M. Sun, R. Qiao, S.E. Renfrew, L. Ma, T. Wu, S. Hwang, D. Nordlund, D. Su, K. Amine, J. Lu, B.D. McCloskey, W. Yang, W. Tong, Nat. Commun. 9 (2018) 947.
[12] K. Luo, M.R. Roberts, R. Hao, N. Guerrini, D.M. Pickup, Y.-S. Liu, K. Edström, J. Guo, A.V. Chadwick, L.C. Duda, P.G. Bruce, Nat. Chem. 8 (2016) 684.
[13] K. Luo, M.R. Roberts, N. Guerrini, N. Tapia-Ruiz, R. Hao, F. Massel, D.M. Pickup, S. Ramos, Y.S. Liu, J. Guo, A.V. Chadwick, L.C. Duda, P.G. Bruce, J. Am. Chem. Soc. 138 (2016) 11211.
[14] W. Li, B. Song, A. Manthiram, Chem. Soc. Rev. 46 (2017) 3006.
[15] E. Hu, X. Yu, R. Lin, X. Bi, J. Lu, S. Bak, K.-W. Nam, H.L. Xin, C. Jaye, D.A. Fischer, K. Amine, X.-Q. Yang, Nat. Energy 3 (2018) 690.
[16] Y. Pei, C.-Y. Xu, Y.-C. Xiao, Q. Chen, B. Huang, B. Li, S. Li, L. Zhen, G. Cao, Adv. Funct. Mater. 27 (2017) 1604349.
[17] P. Yan, J. Zheng, T. Chen, L. Luo, Y. Jiang, K. Wang, M. Sui, J.G. Zhang, S. Zhang, C. Wang, Nat. Commun. 9 (2018) 2437.
[18] P. Yan, J. Zheng, J. Liu, B. Wang, X. Cheng, Y. Zhang, X. Sun4, C. Wang, J.-G. Zhang, Nat. Energy 3 (2018) 600.
[19] D.H. Seo, J. Lee, A. Urban, R. Malik, S. Kang, G. Ceder, Nat. Chem. 8 (2016) 692.
[20] X. Li, Y. Qiao, S. Guo, Z. Xu, H. Zhu, X. Zhang, Y. Yuan, P. He, M. Ishida, H. Zhou, Adv. Mater. 30 (2018) 1705197.
[21] M. Saubanère, E. McCalla, J.M. Tarascon, M.L. Doublet, Energy Environ. Sci. 9 (2016) 984.
[22] Y. Xie, M. Saubanère, M.-L. Doublet, Energy Environ. Sci. (2017) 266.
[23] E. McCalla, A.M. Abakumov, M. Saubanère, D. Foix, E.J. Berg, G. Rousse, J.-M. Tarascon, Science 350 (2015) 1516.
[24] M. Sathiya, A.M. Abakumov, D. Foix, G. Rousse, K. Ramesha, M. Saubanere, M. L. Doublet, H. Vezin, C.P. Laisa, A.S. Prakash, D. Gonbeau, G. VanTendeloo, J. M. Tarascon, Nat. Mater. 14 (2015) 230.
[25] A.J. Perez, Q. Jacquet, D. Batuk, A. Iadecola, M. Saubanère, G. Rousse, D. Larcher, H. Vezin, M.-L. Doublet, J.-M. Tarascon, Nat. Energy 2 (2017) 954.
[26] B. Li, D. Xia, Adv. Mater. 29 (2017) 1701054.
[27] E. McCalla, A.M. Abakumov, M. Saubanère, D. Foix, E.J. Berg, G. Rousse, M.-L. Doublet, D. Gonbeau, P. Novák, G.V. Tendeloo, R. Dominko, J.-M. Tarascon, Science 350 (2015) 1516.
[28] W. Kohn, A.D. Becke, R.G. Parr, J. Phys. Chem. 100 (1996) 12974.
[29] P.E. Blochl, Phys. Rev. B 24 (1994) 17953.
[30] A.I. Liechtenstein, Phys. Rev. B 8 (1995) R5467.
[31] A. Jain, G. Hautier, S.P. Ong, C.J. Moore, C.C. Fischer, K.A. Persson, G. Ceder, Phys. Rev. B 84 (2011), 045115.
[32] G. Hautier, S.P. Ong, A. Jain, C.J. Moore, G. Ceder, Phys. Rev. B 85 (2012) 155208.
[33] J. Heyd, G.E. Scuseria, M. Ernzerhof, J. Chem. Phys. 118 (2003) 8207.
[34] L. Wang, T. Maxisch, G. Ceder, Phys. Rev. B 73 (2006) 195107.
[35] K.K. Banger, Y. Yamashita, K. Mori, R.L. Peterson, T. Leedham, J. Rickard, H. Sirringhaus, Nat. Mater. 10 (2011) 45.
[36] H. Wang, J. Zhang, X. Hang, X. Zhang, J. Xie, B. Pan, Y. Xie, Angew Chem. Int. Ed. Engl. 54 (2015) 1195.
[37] Y. Pei, Q. Chen, Y.-C. Xiao, L. Liu, C.-Y. Xu, L. Zhen, G. Henkelman, G. Cao, Nano Energy 40 (2017) 566.
[38] H. Liu, K.J. Harris, M. Jiang, Y. Wu, G.R. Goward, G.A. Botton, ACS Nano 12 (2018) 2708.
[39] J. Zheng, P. Xu, M. Gu, J. Xiao, N.D. Browning, P. Yan, C. Wang, J.-G. Zhang, Chem. Mater. 27 (2015) 1381.
[40] Z. Wang, D. Santhanagopalan, W. Zhang, F. Wang, H.L. Xin, K. He, J. Li, N. Dudney, Y.S. Meng, Nano Lett. 16 (2016) 3760.
[41] F. Lin, I.M. Markus, D. Nordlund, T.C. Weng, M.D. Asta, H.L. Xin, M.M. Doeff, Nat. Commun. 5 (2014) 3529.

[42] S. Hwang, W. Chang, S.M. Kim, D. Su, D.H. Kim, J.Y. Lee, K.Y. Chung, E.A. Stach, Chem. Mater. 26 (2014) 1084.
[43] P. Yan, J. Zheng, X. Zhang, R. Xu, K. Amine, J. Xiao, J.-G. Zhang, C.-M. Wang, Chem. Mater. 28 (2016) 857–863.
[44] R. Shunmugasundaram, R. Senthil Arumugam, J.R. Dahn, Chem. Mater. 27 (2015) 757.
[45] J.R. Croy, M. Balasubramanian, K.G. Gallagher, A.K. Burrell, Acc. Chem. Res. 48 (2015) 2813.
[46] M. Sathiya, G. Rousse, K. Ramesha, C.P. Laisa, H. Vezin, M.T. Sougrati, M. L. Doublet, D. Foix, D. Gonbeau, W. Walker, A.S. Prakash, M. Ben Hassine, L. Dupont, J.M. Tarascon, Nat. Mater. 12 (2013) 827.
[47] T. Zhao, L. Li, R. Chen, H. Wu, X. Zhang, S. Chen, M. Xie, F. Wu, J. Lu, K. Amine, Nano Energy 15 (2015) 164.
[48] Q. Xia, X. Zhao, M. Xu, Z. Ding, J. Liu, L. Chen, D.G. Ivey, W. Wei, J. Mater. Chem. A. 3 (2015) 3995.
[49] H. Chen, M.S. Islam, Chem. Mater. 28 (2016) 6656–6663.
[50] D. Mohanty, J. Li, D.P. Abraham, A. Huq, E.A. Payzant, D.L. Wood, C. Daniel, Chem. Mater. 26 (2014) 6272.
[51] M. Ben Yahia, J. Vergnet, M. Saubanere, M.L. Doublet, Nat. Mater. 18 (2019) 496.